ROS-sensitive thioketal-linked polyphosphoester-doxorubicin conjugate for precise phototriggered locoregional chemotherapy

Pei Pei[a,1], Chunyang Sun[b,1], Wei Tao[a,1], Jie Li[a], Xianzhu Yang[a,c,*], Jun Wang[c,d,f,**]

[a] School of Biological and Medical Engineering, Hefei University of Technology, Hefei, Anhui, 230009, PR China
[b] Department of Radiology and Tianjin Key Laboratory of Functional Imaging, Tianjin Medical University General Hospital, Tianjin, 300052, PR China
[c] Institutes for Life Sciences, School of Medicine, South China University of Technology, Guangzhou, Guangdong, 510006, PR China
[d] National Engineering Research Center for Tissue Restoration and Reconstruction, South China University of Technology, Guangzhou, Guangdong, 510006, PR China
[f] Guangdong Key Laboratory of Nanomedicine, Shenzhen Institutes of Advanced Technology, Chinese Academy of Sciences, Shenzhen, 518055, PR China

ARTICLE INFO

ABSTRACT

Minimizing drug leakage at off-target sites and triggering sufficient drug release in tumor tissue are major objectives for effective nanoparticle (NP)-based cancer therapy. The current covalent and cleavable drug-NP conjugation strategy is promising but lacks high controllability to realize tumor-specific release. As a proof-of-concept, the reactive oxygen species (ROS)-activatable thioketal (TK) bond was explored as the linkage between doxorubicin (DOX) and polyphosphoester (PPE-*TK*-DOX). The Ce6@PPE-*TK*-DOX NPs constructed by co-self-coassembly of PPE-*TK*-DOX and the photosensitizer Ce6 efficiently prevented premature drug leakage in the off-target tissue and cells because of the high stability of the TK bond under physiological conditions. Once circulating into the tumor site, the 660-nm red light was precisely employed to irradiate the tumor area under the guidance of fluorescence/magnetic resonance (MR) dual-model imaging, which can induce localized ROS generation, resulting in rapid cleavage of the TK bond. Consequently, the DOX prodrug was locoregionally released and activated, achieving tumor-specific drug delivery with high controllability by light. Such phototriggered prodrug release and activation at the desired site significantly enhanced the therapeutic efficacy and minimized the side effect, providing new avenues to develop drug delivery systems for remote on-demand drug delivery *in vivo*.

1. Introduction

Currently, nanocarriers offer the capability to preferentially deliver cytotoxic drugs to tumors due to the enhanced permeability and retention (EPR) effect, leading to a potentially enhanced anticancer effect [1–4]. An ideal nanocarrier should stably hold the drug in the bloodstream and healthy tissue to minimize drug leakage and reduce cytotoxic effects [5–7]. Once it has reached the tumor, the nanocarrier is susceptible to specific release of sufficient drug in cancer cells to efficiently induce cancer cell apoptosis [8–11]. Although such a design principle is well understood, currently available nanocarriers cannot adequately fulfill these requirements [12,13]. This opens up a new challenge to explore nanocarriers with highly controllable locoregional drug release properties that can deliver cytotoxic drug to the desire sites while minimizing its activity at off-target sites.

It is well known that physical encapsulation and chemical conjugation are two major methods to load drug molecules. The drug-encapsulated formulation usually has inevitable drug leakage during circulation, making it difficult to achieve the highly controllable locoregional drug release [14,15]. The alternative strategy is the covalent conjugation of drug molecules to nanocarriers *via* a biodegradable linkage that is stable in circulation to prevent undesired drug leakage but susceptible to specific degradation to enable controllable drug release within tumor cells [16–18]. Various covalent linkages between drugs and nanocarriers have been explored to realize such tumor-specific release. Among them, cleavable linkers that are sensitive to endo/lysosomal acid, intracellular reductive environment, or specific intracellular enzymes are used most frequently [19–23]. However, it should be noted that the intracellular endo/lysosomal acidic and reductive environment also exists in normal cells, resulting in undesired release in off-target cells [24]. For the enzyme-responsive formulations, certain enzymes should be specifically expressed, and their

---

concentrations should also be sufficient to disrupt the linkers. However, convincing evidence has indicated the existence of significant heterogeneity for the expression of these enzymes that are dynamically changed in different tumor patients or the same individual at different tumor stages [25,26]. Thus, exploring highly controllable cleavable linkers to specifically release cytotoxic drugs within tumor cells is still urgently desired.

Recently, red or near-infrared (NIR) light with wavelengths in the range of approximately 650–950 nm has emerged as an attractive external stimulus for biomedical applications because of its spatiotemporal controllability, high tissue penetrability, and minimal phototoxicity [27–29]. However, the low energy of the red and NIR light could indirectly cleave the chemical bond [30–32]. Fortunately, under the assistance of photosensitizers, the red light efficiently generates reactive oxygen species (ROS) [33,34], which readily cleave numerous covalent bonds, including thioketal [35,36], phenylboronic ester [37], and diselenide bonds [38]. Thus, the cytotoxic anticancer drug doxorubicin (DOX) was conjugated to the side chain of polyphosphoesters (PPEs) by a thioketal bond (PPE-*TK*-DOX), which could simultaneously encapsulate the photosensitizer Ce6 during its self-assembly in aqueous solution (Fig. 1). The obtained Ce6@PPE-*TK*-DOX nanoparticles (NPs) avoid premature drug release completely during blood circulation because of the high stability of the thioketal bond under physiological conditions. Under fluorescence/magnetic resonance (MR) dual-model imaging-guided illumination, the conjugated DOX prodrug was locoregionally released and activated at the tumor site by the generated ROS. Such a locoregionally activated chemotherapy strategy efficiently minimized nonspecific cytotoxicity to healthy tissue and realized specific chemotherapy for cancer treatment.

2. Materials and methods

2.1. Materials

Doxorubicin hydrochloride (DOX•HCl) and chlorin e6 (Ce6) were obtained from Zhejiang Hisun Pharmaceutical Co., Ltd. (China). Dulbecco's Modified Eagle's Medium (DMEM) and fetal bovine serum (FBS) were obtained from Gibco BRL (Eggenstein, Germany). 3-(4,5-Dimethylthiazol-2-yl)-2,5-diphenyl tetrazolium bromide (MTT), Alexa Fluor® 488 phalloidin and 4,6-diamidino-2-phenylindol (DAPI) were purchased from Sigma-Aldrich (St Louis, MO, USA). Other reagents and organic solvents were of analytical grade and used as received. The cyclic phosphoester monomers PPEG and AEP were synthesized as previously described in the literature [13,39]. The synthesis processes of $P(PPEG_{10}\text{-}co\text{-}AEP_{20})$, $P(PPEG_{10}\text{-}co\text{-}AEP(Cya)_{20})$ and PPE-*TK*-DOX were described in the supporting information. Other organic solvents or reagents were of analytic grade and used as received.

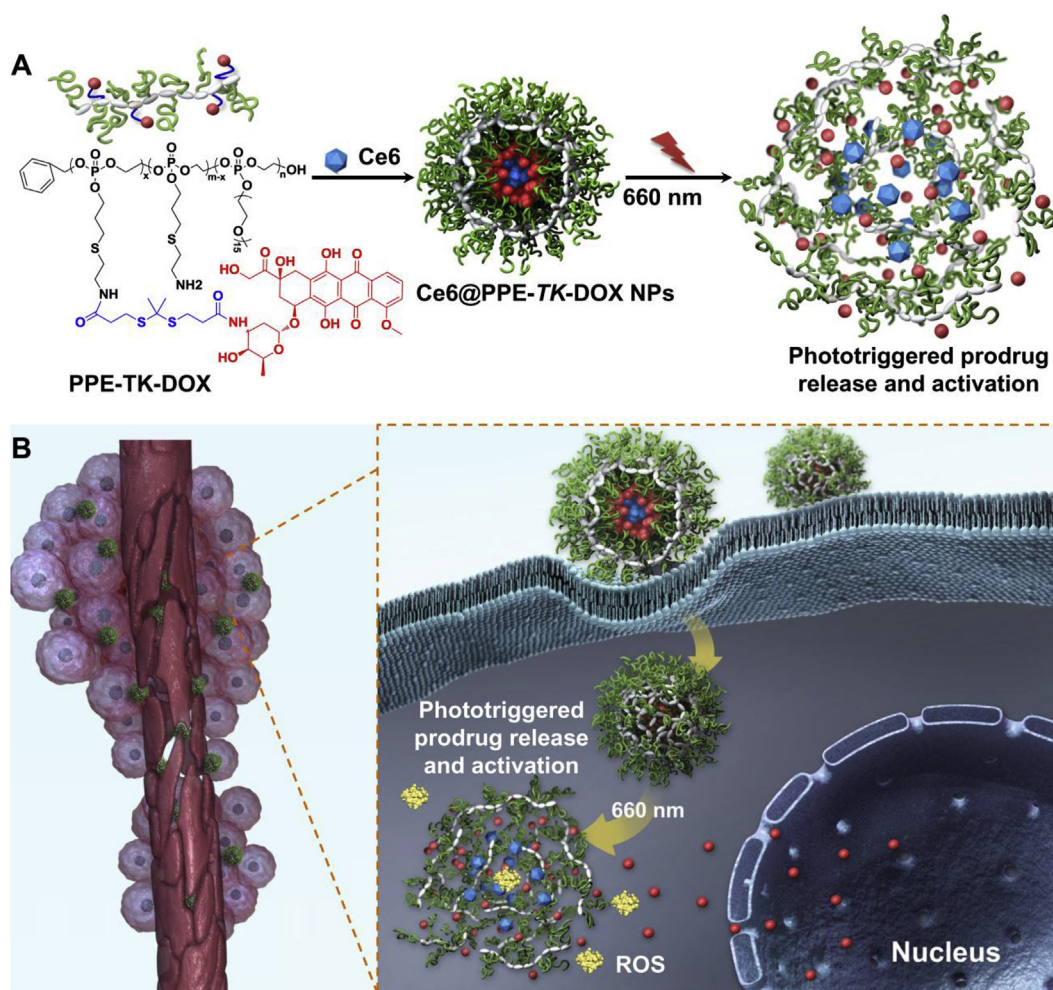**Fig. 1.** Schematic illustration of the Ce6@PPE-*TK*-DOX NPs for phototriggered prodrug release and activation. (A) The Ce6@PPE-*TK*-DOX NPs was constructed by co-self-coassembly of PPE-*TK*-DOX and photosensitizer Ce6, which efficiently prevented premature drug leakage in the off-target tissue and cells. (B) In the tumor site, the 660-nm red light irradiation can induce localized ROS generation, resulting in the rapid cleavage of TK bond and DOX prodrug release for locoregionally activated chemotherapy. (For interpretation of the references to colour in this figure legend, the reader is referred to the Web version of this article.)

2.2. Characterization

The molecular weights of the samples were measured on a Waters gel permeation chromatography (GPC) system. NMR spectra were recorded in deuterated reagent using an Agilent VNMRS 600 MHz NMR spectrometer (California, USA). The size and size distribution of the samples were measured using dynamic light scattering (DLS) (NanoBrook-90 Plus instrument, Brookhaven Instrument Corporation, Holtsville, New York, USA). The morphology of samples was analyzed using JEM-2100F transmission electron microscopy (TEM) at an accelerating voltage of 200 kV. The fluorescence of DOX was detected by a fluorospectrophotometer (λ_{ex} = 460 nm, Hitachi F-7000, Japan). The absorption spectra were measured by a UV-3802 spectrophotometer (UNICO, Shanghai, China). The concentrations of DOX and Ce6 were determined by HPLC and UV–Vis spectroscopy, as previously reported.

2.3. Preparation of Ce6-loaded nanoparticles

The Ce6@PPE-*TK*-DOX NPs were prepared by a dialysis method. Briefly, PPE-*TK*-DOX (10.0 mg) and Ce6 (0.25, 0.5, 0.75, 1.0, 1.5, or 2.0 mg) were dissolved in tetrahydrofuran (1.0 mL) and then added dropwise in 10.0 mL of ultrapure water under stirring for 6 h in the dark. Thereafter, the mixture solution was transferred to a dialysis tube (cut-off molecular weight was 14,000 Da) to dialyze against ultrapure water overnight. Next, the unloaded Ce6 was removed using a 0.45-μm filter (Millipore). Similarly, PPE-*TK*-DOX NPs were prepared in the absence of Ce6.

2.4. Nanoparticle stability

Ce6@PPE-*TK*-DOX NPs and PPE-*TK*-DOX NPs were incubated in PBS with 10% FBS or PBS. After incubation for seven days, the diameters were measured everyday by DLS.

2.5. In vitro phototriggered DOX release

The solutions of Ce6@PPE-*TK*-DOX NPs or free Ce6 + PPE-*TK*-DOX NPs (1.0 mL, [DOX] = 179.7 μg/mL, [Ce6] = 24.4 μg/mL) were transferred into the dialysis membrane tubing (MWCO 14000 Da) and then were immersed in the PB buffer (0.02 M, pH 7.4, 15 mL) with gentle shaking (80 rpm) at 37 °C. At 4, 28, or 52 h, the solution was transferred into a centrifuge tube, incubated in a water bath at 37 °C, irradiated with a 660-nm laser (0.1 W/cm²) for 10 min, and then transferred back to the dialysis membrane tubing. Both formulations without illumination were used as controls. At predetermined intervals, the external PBS was collected and replaced with fresh PBS. The collected solution of DOX was lyophilized and analyzed by high-performance liquid chromatography (HPLC) to determine the concentration [35].

2.6. Degradation of the thioketal linker under 660-nm light

Briefly, Ce6@PPE-*TK*-DOX NPs and free Ce6 + PPE-*TK*-DOX NPs were suspended in phosphate buffer at pH 7.4 at a Ce6 concentration of 2.5 μg/mL. The nanoparticles were then exposed to a 660-nm laser at a power density of 0.1 W/cm². The resultant thiol groups were detected by 5,5′-dithiobis(2-nitrobenzoic acid) (DTNB) at degradation rates of 20, 40, and 60 min, as reported in a previous study [36].

2.7. In vitro generation of ROS

Ce6@PPE-*TK*-DOX NPs or Ce6 + PPE-*TK*-DOX NPs ([Ce6] = 30.0 μg/mL, 100 μL of each solution) were mixed with 9,10-anthracenediyl-bis(methylene) dimalonic acid (ABDA, 0.1 mg/mL; 2.0 mL) in PBS (pH 7.4) solution and then were irradiated with a 660-nm laser for different periods of time at a power density of 0.1 W/cm². The ABDA absorption decrease at 379 nm was determined to reflect the production of ROS because ABDA can efficiently trap ROS by fast reaction with the anthracene moiety.

2.8. Intracellular DOX release under irradiation

MDA-MB-231 cells were seeded in 24-well plates (1×10^5 cells/well) and were incubated at 37 °C for 24 h. Thereafter, fresh DMEM medium containing Ce6@PPE-*TK*-DOX NPs or Ce6 + PPE-*TK*-DOX NPs ([DOX] = 2.0 μg/mL, [Ce6] = 0.27 μg/mL) were added to replace the original medium. After incubation for 4 h, the MDA-MB-231 cells were washed twice with PBS and then were exposed to a 660-nm laser for 30 min at a power density of 0.1 W/cm². MDA-MB-231 cells incubated with Ce6@PPE-*TK*-DOX NPs or Ce6 + PPE-*TK*-DOX NPs without irradiation were also used as the control group. After incubation for another 4 h, the cells were washed twice, trypsinized, collected, and suspended in PBS for FACS. In addition, to quantify the intracellular DOX content, the cells was treated as described above, and then the cells were collected and lyophilized for HPLC analysis as reported previously [35].

For CLSM observations, MDA-MB-231 cells were seeded on coverslips in 24-well plates (5×10^4 cells/well) at 37 °C for 24 h, and then the medium was replaced with fresh DMEM medium containing Ce6@PPE-*TK*-DOX NPs or Ce6 + PPE-*TK*-DOX NPs ([DOX] = 5.0 μg/mL, [Ce6] = 0.69 μg/mL). After incubation for 4 h at 37 °C, the MDA-MB-231 cells were washed twice with PBS and exposed to a 660-nm laser for 30 min at a power density of 0.1 W/cm². Thereafter, the cells were incubated for another 4 h, washed with PBS, and fixed with 4% formaldehyde at room temperature for 20 min. Subsequently, the cell nuclei and cytomembranes were counterstained with DAPI and Alexa Fluor 488 phalloidin for CLSM observation (LSM 710, Carl Zeiss, Inc., Jena, Germany).

2.9. In vitro cytotoxicity studies

MDA-MB-231 cells were seeded into 96-well plates (5.0×10^3 cells/well) and incubated for 24 h at 37 °C. Next, the medium was replaced with fresh DMEM medium containing Ce6@PPE-*TK*-DOX NPs or Ce6 + PPE-*TK*-DOX NPs at different concentrations. After incubation for 4 h at 37 °C, the cells were washed twice with PBS and were irradiated with a 660-nm laser in an incubator for 30 min at a power of 0.1 W/cm². Thereafter, the cells were further incubated for 48 h at 37 °C, and then the 3-(4,5-dimethylthiazol-2-yl)-2,5-diphenyltetrazolium bromide (MTT) assay was performed to measure the cell viability according to the standard protocol.

2.10. Apoptosis assay

MDA-MB-231 cells were seeded into 24-well plates (5×10^4 cells/well) and incubated for 24 h at 37 °C. Subsequently, the medium was replaced with fresh DMEM medium containing Ce6@PPE-*TK*-DOX NPs or Ce6 + PPE-*TK*-DOX NPs ([DOX] = 1.25 μg/mL, [Ce6] = 0.17 μg/mL). After incubation for 4 h at 37 °C, the cells were washed twice with PBS and irradiated by a 660-nm laser in an incubator for 30 min at a power of 0.1 W/cm². Thereafter, the cells were incubated for an additional 24 h at 37 °C. Finally, the cells were trypsinized, centrifuged, collected and treated according to the procedure suggested in the Annexin V-FITC apoptosis detection kit I (BD Biosciences). The results were analyzed using FlowJo® V10 software.

2.11. Animal and tumor models

Female BALB/c nude mice (20 ± 2 g, 6 weeks old) were purchased from Beijing HFK Bioscience Co. Ltd., and all animals received care in compliance with the guidelines outlined in the Guide for the Care and Use of Laboratory Animals. The procedures were approved by the Hefei University of Technology Animal Care and Use Committee. MDA-MB-

231 cells (5×10^6) cells were injected into the mammary fat pads to establish a human breast cancer xenograft tumor model, and when the tumor volumes reached $100\,mm^3$, the mice were used for subsequent experiments.

2.12. Pharmacokinetic and biodistribution studies

Mice bearing MDA-MB-231 tumors were randomly divided into three groups (n = 4 per group) and then intravenously injected with free DOX, Ce6 + PPE-*TK*-DOX NPs and Ce6@PPE-*TK*-DOX NPs *via* the tail vein at a DOX dose of 10 mg/kg. At predetermined time points, blood was collected from the retro-orbital plexus of the mouse eye, and plasma was obtained by centrifugation in heparinized tubes. The concentration of DOX in the plasma of each group was measured according to a previously reported method. Pharmacokinetic parameters were calculated by the non-compartmental data analysis of blood concentrations.

Nude mice bearing MDA-MB-231 tumors were treated with an equivalent DOX injection as described above. The mice were then sacrificed, and the main organs or solid tumor tissues were harvested after 12 h or 24 h to measure the DOX accumulation by HPLC [40].

2.13. In vivo fluorescence and MR imaging

Following the intravenous injection of Ce6@PPE-*TK*-DOX NPs into nude mice bearing MDA-MB-231 xenografts at a DOX dosage of 5.0 mg/kg, the *in vivo* fluorescence distribution in tumor-bearing mice was detected at predetermined time points using a Xenogen IVIS® Lumina system (Caliper Life Sciences, USA). At 24 h post-injection, the mice were sacrificed, and the solid tumor tissues were collected, washed with PBS, and imaged using the Xenogen IVIS Lumina system.

Furthermore, to evaluate *in vivo* tumor MR imaging, Ce6-Gd@PPE-*TK*-DOX NPs at a DOX dosage of 5.0 mg/kg, was intravenously injected into the mice bearing MDA-MB-231 tumors. Next, the tumor region of the mice was observed using a 3.0 T clinical MR system with a small animal receiver coil (GE Signa Excite). The imaging intensity at the tumor was analyzed at different time points.

2.14. In vivo antitumor efficacy

The nude mice bearing MDA-MB-231 tumors were randomly divided into six groups (n = 5 per group) and intravenous injected with Ce6@PPE-*TK*-DOX NPs, Ce6 + PPE-*TK*-DOX NPs, free DOX, or free Ce6 at the dosages of DOX and Ce6 of 5.0 mg/kg and 0.69 mg/kg, respectively. After 24 h post-administration, the tumor site was irradiated under a 660-nm laser for 30 min at a power density of $0.1\,W/cm^2$; the groups without irradiation were used as controls. The mice received treatments as described above twice a week. The size of the tumors was monitored using calipers by measuring the perpendicular diameter, and the volume was calculated using the following equation: tumor volume = (length * width^2)/2. After 16 days, the mice were sacrificed, and the solid tumor tissues were excised and weighed.

2.15. Immunohistochemical analysis

After the last injection, the tumor tissues were excised from the sacrificed mice, weighed, fixed in 4% formaldehyde and embedded in paraffin for immunnohistochemical staining using the proliferating cell nuclear antigen (PCNA) assay.

2.16. Statistical analysis

Statistical significance of the treatment groups was evaluated using Student's t-*test*. *p values < 0.05 and **p values < 0.01 were considered statistically significant in all analyses.

3. Results and discussion

To substantiate our design, the PPE-*TK*-DOX conjugate was obtained using a multiple synthesis process as shown in Scheme S1. First, the random copolymer of the polyphosphoester P(PPEG$_{10}$-*co*-AEP$_{20}$) was synthesized by ring-opening polymerization of the cyclic phosphoester monomers AEP and PPEG. The successful synthesis was verified by gel permeation chromatography (GPC, Fig. S1) and ^{1}H NMR spectroscopy (Fig. S2). Thereafter, the allyl groups of P(PPEG$_{10}$-*co*-AEP(Cya)$_{20}$) were converted to amino groups *via* the thiol-ene reaction with cysteamine, and the transformation efficacy was approximately 100% according to ^{1}H NMR analysis (Fig. S2). Subsequently, the ROS-activatable DOX prodrug (DOX-*TK*) synthesized by coupling DOX with a ROS-cleavable thioketal (TK) was conjugated to partial amino groups of poly(PPEG$_{10}$-*co*- AEP(Cya)$_{20}$) to obtain PPE-*TK*-DOX. The extent of DOX conjugation was approximately 35.3% according to ^{1}H NMR analysis (Fig. S3). Additionally, the DOX content of PPE-*TK*-DOX was also determined according to its UV–vis absorbance at 490 nm, calculated to be ~20.2%, corresponding to a conjugation efficiency of 35.3%, which is well consistent with the ^{1}H NMR result in Fig. S3. The critical micelle concentration of PPE-*TK*-DOX was calculated as 1.5×10^{-3} mg/mL (Fig. S4).

Thereafter, the synthesized amphiphilic PPE-*TK*-DOX also formed nanoparticles (PPE-*TK*-DOX NPs) in aqueous solution because of the hydrophobic nature of the DOX residue, and its diameter measured by dynamic light scattering (DLS) was ~70 nm (Fig. 2A). Meanwhile, the PPE-*TK*-DOX and hydrophobic photosensitizers chlorin e6 (Ce6) can co-self-assemble into nanoparticles (Ce6@PPE-*TK*-DOX NPs) with a slightly larger diameter of ~73 nm in aqueous solution. The loading content of Ce6 in Ce6@PPE-*TK*-DOX NPs increased as Ce6/PPE-*TK*-DOX feed ratio increased (Fig. S5), reaching 2.74 ± 0.13% at the feed ratio of 10:1 (wt./wt.), which was used in the subsequent experiments. Both nanoparticles maintained their diameters for over 7 days (Fig. 2B) in phosphate buffered saline (PBS) or PBS containing 10% fetal bovine serum (FBS), which may have been due to the PEG side chain of PPE-*TK*-DOX. The similar UV–vis absorption of the Ce6@PPE-*TK*-DOX (Fig. 2C) NPs exhibited a slight redshift for the conjugated DOX and encapsulated Ce6, suggesting the occurrence of intermolecular π–π stacking interactions between DOX and Ce6, enhancing the stability of Ce6@PPE-*TK*-DOX NPs.

According to our design, red light irradiation with a wavelength of 660 nm would generate ROS by the encapsulated Ce6, leading to rapid cleavage of the TK bond of the DOX prodrug, resulting in photo-triggered drug release. Thus, Ce6@PPE-*TK*-DOX NPs was irradiated with three laser on (L+, 10 min)/laser off (L-, 24 h) input cycles by a 660-nm laser at a power density of $0.1\,W/cm^2$. Additionally, free Ce6 and PPE-*TK*-DOX NPs (Ce6 + PPE-*TK*-DOX NPs) that separately dispersed in the buffer solution were used as a control. Furthermore, both formulations without illumination were used as control formulations. As shown in Fig. 2D, DOX release from Ce6@PPE-*TK*-DOX nanoparticles occurred in a triggered and stepwise-dependent manner. During the first input cycle, 22.7% of DOX was suddenly released. Such phototriggered drug release was observed plus the same repeated illumination, and bursts of DOX release reached 41.2% and 56.9% during the second and third cycles, respectively. By contrast, DOX release from Ce6@PPE-*TK*-DOX NPs almost completely stopped in the absence of illumination (Ce6@PPE-*TK*-DOX NPs (L-)). In addition, less than 10% of DOX was released from the Ce6 + PPE-*TK*-DOX NPs with illumination, although more ROS were generated than those from Ce6@PPE-*TK*-DOX NPs (Fig. S6).

To elucidate the mechanism underlying phototriggered prodrug release, the sizes and morphologies change of these samples after three laser on/laser off input cycles were first observed *via* DLS and transmission electron microscopy (TEM) imaging. As shown in Figs. 2E and 660-nm laser irradiation induced the size decrease in Ce6@PPE-*TK*-DOX NPs from ~73 nm to ~25 nm, while such a size change was not
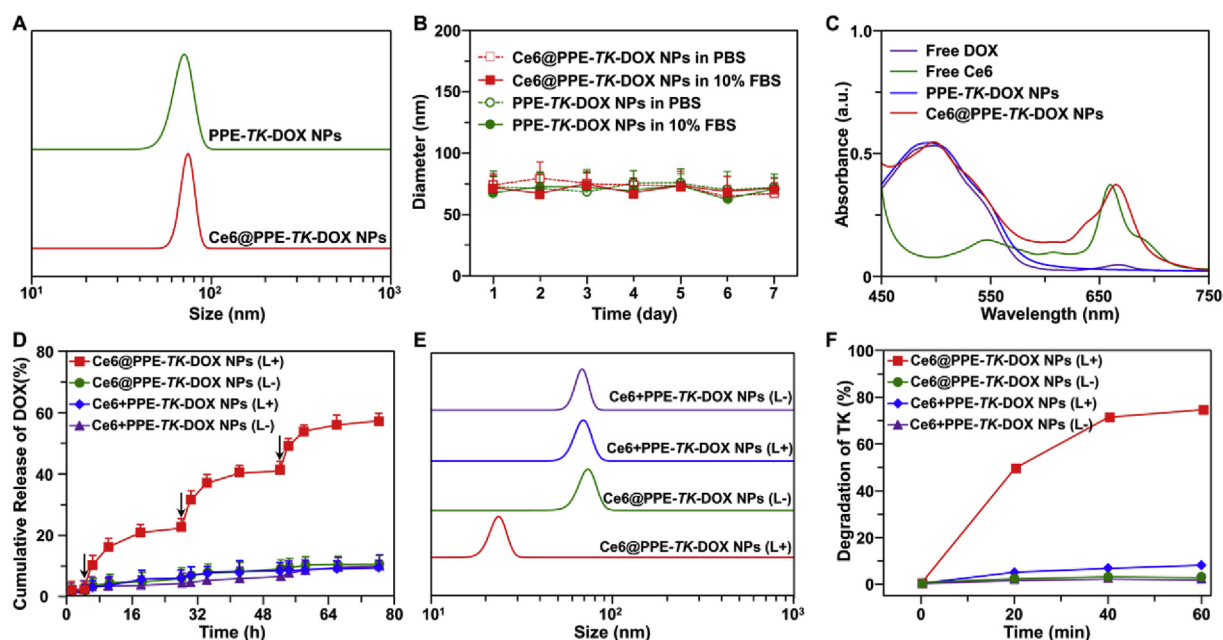
Fig. 2. Preparation and characterization of the nanoparticles Ce6@PPE-*TK*-DOX NPs for phototriggered prodrug release and activation. (A, B, C) Particle size distribution (A), stability (B), and UV–vis–NIR absorption spectra (C) of Ce6@PPE-*TK*-DOX NPs and the control formulations. (D) DOX release profiles of Ce6@PPE-*TK*-DOX NPs and the control formulation Ce6 + PPE-*TK*-DOX NPs during the three laser on/laser off input cycle. The black arrows indicated the laser on (660 nm, 0.1 W/cm^2). (E, F) The size changes and TK linker degradation of Ce6@PPE-*TK*-DOX NPs and Ce6 + PPE-*TK*-DOX NPs with or without 660-nm laser irradiation.

observed for the Ce6 + PPE-*TK*-DOX NPs(L +) group. This size decrease under illumination was also confirmed using TEM imaging (Fig. S7), in which small particles less than 30 nm and the destructing nanostructure were observed only in the Ce6@PPE-*TK*-DOX NPs(L +) group after 660-nm laser irradiation. By contrast, the illumination showed a negligible effect on the size and morphology of Ce6 + PPE-*TK*-DOX NPs. In addition, we evaluated the cleavage of TK bonds under illumination. As reported, the TK bond was converted to two thiol terminal groups by ROS [36]. Thus, the degradation rate of the TK bond was calculated by measuring the amount of thiol groups by Ellman's test. As shown in Fig. 2F, the degradation of the TK bond was not observed without illumination for Ce6@PPE-*TK*-DOX NPs and Ce6 + PPE-*TK*-DOX NPs. Notably, the degradation ratios of the TK bond of Ce6@PPE-*TK*-DOX NPs were significantly increased with the extension of the irradiation times. It could be clearly observed that approximately 49.3% and 71.3% of the TK bonds of Ce6@PPE-*TK*-DOX NPs were cleaved after receiving 660-nm laser irradiation for 20 and 40 min, respectively. By contrast, less than 10% of TK bonds of Ce6 + PPE-*TK*-DOX NPs were degraded under illumination for 60 min. Therefore, it could be speculated that the encapsulation of Ce6 in PPE-*TK*-DOX NPs was a prerequisite for the degradation of the TK bond and subsequent phototriggered-conjugated DOX release, which could be due to the short action distance (< 20 nm) and limited lifetime (< 40 ns) of ROS [35]. By contrast, the phototriggered DOX prodrug release was not observed when free Ce6 and PPE-*TK*-DOX NPs were separately dispersed because the generated ROS by free Ce6 inefficiently cleaved the TK bond of PPE-*TK*-DOX NPs.

Based on the above results, it can be concluded that the conjugation of DOX into the side chain of PPE *via* the TK bond could efficiently avoid premature drug release. The conjugated DOX prodrug can be efficiently released from Ce6@PPE-*TK*-DOX NPs because the ROS generated *in situ* by the encapsulated Ce6 under illumination can efficiently cleave the surrounding TK linker and destruct the nanostructure of Ce6@PPE-*TK*-DOX NPs.

Inspired by the phototriggered DOX prodrug activation and release, we next investigated the effect of illumination on the intracellular DOX distribution in MDA-MB-231 cells. After pre-incubation with Ce6@PPE-

TK-DOX NPs or Ce6 + PPE-*TK*-DOX NPs for 4 h, the MDA-MB-231 cells were washed with PBS to remove the noninternalized nanoparticles and then exposed to a 660-nm laser at a power density of 0.1 W/cm^2 for 30 min. After further incubation for 4 h, the intracellular DOX fluorescence indensities and contents were analyzed using FACS (Accuri C6 flow cytometer, BD Biosciences, USA) and HPLC analyses. Fig. 3A and Fig. S8 demonstrate that much stronger fluorescence intensities of DOX were observed in cells treated with Ce6@PPE-*TK*-DOX NPs(L +) than in those without illumination. By contrast, the cells incubated with Ce6 + PPE-*TK*-DOX NPs(L +) irradiation exhibited no obvious increase in fluorescence intensity. However, the intracellular DOX content was comparable when the cells were treated with Ce6@PPE-*TK*-DOX NPs or Ce6 + PPE-*TK*-DOX NPs, and the 660-nm light irradiation was also negligibly affected by the intracellular DOX content (Fig. 3B). To demonstrate the reason for this result, we detected the DOX fluorescence spectra of Ce6@PPE-*TK*-DOX NPs and Ce6 + PPE-*TK*-DOX NPs, and free DOX at an equivalent concentration was used as a control. The DOX fluorescence was clearly partially quenched after assembly into nanoparticles for both Ce6@PPE-*TK*-DOX NPs and Ce6 + PPE-*TK*-DOX NPs (Fig. S9). Therefore, the enhanced intracellular DOX fluorescence should be due to the phototriggered release of DOX prodrug from Ce6@PPE-*TK*-DOX NPs, which resluted in the DOX fluorescence recovery.

Inspired by phototriggered intracellular prodrug release from Ce6@PPE-*TK*-DOX NPs, we next investigated the DOX distribution using CLSM examination. It has been well recognized that only free DOX molecules readily enter nuclei, and they remain in nuclei rather than in the cytoplasm. Without light irradiation, the red fluorescence of DOX was found surrounding the nuclei of MDA-MB-231 cells (Fig. 3C), implying that both Ce6@PPE-*TK*-DOX NPs and Ce6 + PPE-*TK*-DOX NPs were entrapped in the lysosomal vesicles and could stably hold the prodrug. Upon illumination, noticeable red fluorescence could also be observed within the nuclei after MDA-MB-231 cells were incubated with Ce6@PPE-*TK*-DOX NPs, indicating that the intracellularly released prodrug triggered by 660-nm light was already translocated into the nuclei. By contrast, negligible red fluorescence signals were observed in cell nuclei when the cells were treated with Ce6 + PPE-*TK*-DOX NPs and illumination. These results were consistent with the phototriggered
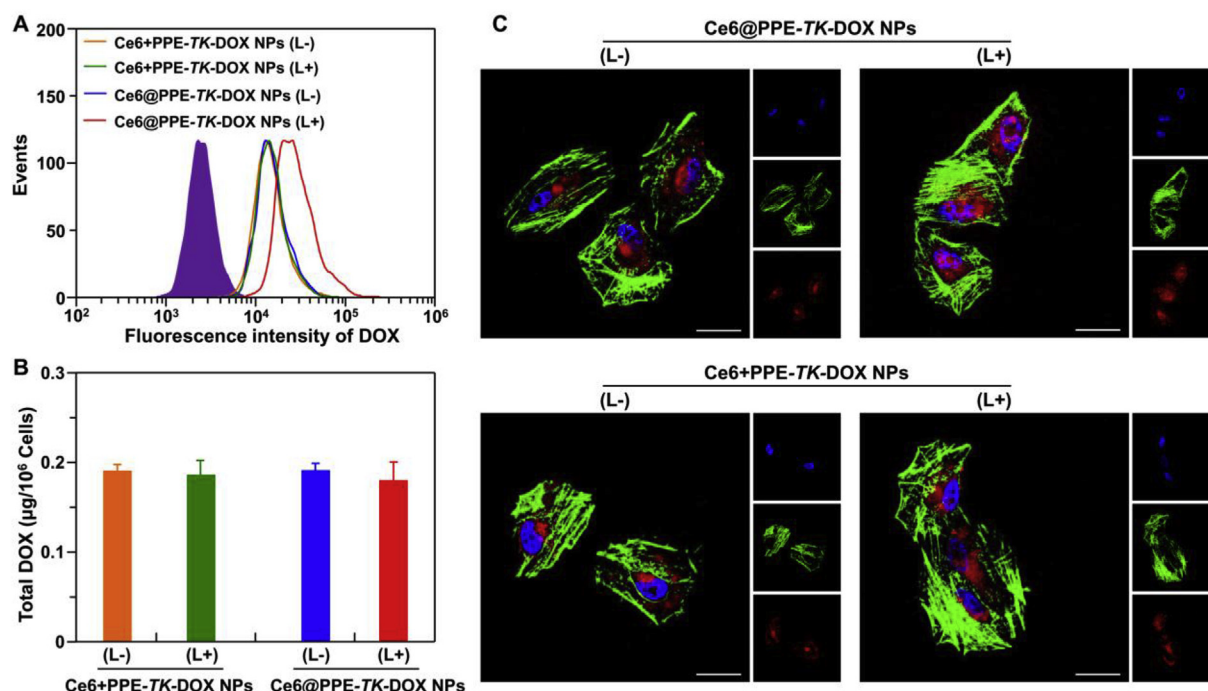
Fig. 3. The phototriggered intracellular DOX prodrug release and activation from Ce6@PPE-*TK*-DOX NPs. (A) Flow cytometric analyses of MDA-MB-231 cells after 660-nm laser irradiation (0.1 W/cm^2, 30 min) and further incubation for 4 h. The MDA-MB-231 cells were pre-cultured with Ce6@PPE-*TK*-DOX NPs or Ce6 + PPE-*TK*-DOX NPs for 4 h. (B) HPLC quantitative analyses of the DOX contents of MDA-MB-231 cells after incubation with Ce6@PPE-*TK*-DOX NPs or Ce6 + PPE-*TK*-DOX NPs for 4 h. (C) CLSM images of MDA-MB-231 cells after 660 nm laser irradiation (0.1 W/cm^2, 30 min) and further incubation for 4 h. The MDA-MB-231 cells were pre-cultured with these formulations for 4 h. Cell nuclei and cytomembrane were counterstained with DAPI (blue) and Alexa Fluor 488 (green). The scale bar is 10 μm. (For interpretation of the references to colour in this figure legend, the reader is referred to the Web version of this article.)

release profile (Fig. 2D).

The enhanced accumulation of DOX in the cell nuclei has been demonstrated to be beneficial in terms of improving the anti-pro-liferation activity of cancer cells. Thus, the cytotoxicities of the abovementioned formulations were examined in MDA-MB-231 cells using the 3-(4,5-dimethylthiazol-2-yl)-2,5-diphenyltetrazolium bro-mide (MTT) assay. After incubation with Ce6@PPE-*TK*-DOX NPs or Ce6 + PPE-*TK*-DOX NPs for 4 h, the non-internalized NPs were re-moved as described above. Next, the cells were illuminated at 660 nm (0.1 W/cm^2) for 30 min and further cultured for 48 h for the MTT assay. At each concentration, treatment with only Ce6@PPE-*TK*-DOX NPs or Ce6 + PPE-*TK*-DOX NPs inefficiently inhibited the proliferation activity of tumor cells (Fig. 4A), indicating the low cytotoxicity of the prodrug without illumination. Upon laser irradiation, the Ce6 + PPE-*TK*-DOX NPs(L+) exhibited slightly enhanced anticancer activity. By contrast, Ce6@PPE-*TK*-DOX NPs(L+) displayed the highest efficacies for in-hibiting tumor cell growth, while the anticancer activity of Ce6@PPE-*TK*-DOX NPs(L+) was obviously decreased with the addition of ROS scavenger vitamin C (V$_C$), indicating that the highest anticancer activity of Ce6@PPE-*TK*-DOX NPs(L+) was due to the combination of photo-triggered DOX prodrug release and the photocytotoxicity of generated ROS.

Furthermore, cell apoptosis by staining with Annexin-V FITC and propidium iodide (PI) was also detected by apoptosis after treatment as mentioned above at an equivalent DOX concentration. As shown in Fig. 4B, Ce6 + PPE-*TK*-DOX NPs(L-) and Ce6@PPE-*TK*-DOX NPs(L-) induced apoptosis in 8.44% and 17.59% of the MDA-MB-231 cells, re-spectively. The percentage of apoptotic cells was moderately elevated to 16.15% when the MDA-MB-231 cells were treated with Ce6 + PPE-*TK*-DOX NPs(L+). Moreover, treatment with Ce6@PPE-*TK*-DOX NPs (L+) induced 66.37% cell apoptosis, which was the highest apoptotic ratio among these treatments. Similarly, the presence of V$_C$ obviously decreased the cell apoptosis of Ce6@PPE-*TK*-DOX NPs(L+) groups by

quenching the generated ROS under illumination.

Given the superior stability in the physiological environment and phototriggered prodrug release property of Ce6@PPE-*TK*-DOX NPs *in vitro*, its pharmacokinetics profile was evaluated. Mice bearing MDA-MB-231 tumors were intravenously injected with Ce6@PPE-*TK*-DOX NPs, Ce6 + PPE-*TK*-DOX NPs, or free DOX, and the concentration of DOX *versus* time was determined using high-performance liquid chro-matography (HPLC). Fig. 5A indicated that Ce6@PPE-*TK*-DOX NPs and Ce6 + PPE-*TK*-DOX NPs exhibited similar pharmacokinetic curves, and both formulations significantly prolonged the circulation of DOX pro-drug in the blood compared with that of free DOX. Furthermore, we calculated the pharmacokinetic parameters of these formulations using a non-compartment model. Fig. 5B demonstrates that the blood clear-ance of Ce6@PPE-*TK*-DOX NPs (0.31 mL/h) and Ce6 + PPE-*TK*-DOX NPs (0.29 mL/h) was much slower than that of free DOX (3.28 mL/h). In addition, Ce6@PPE-*TK*-DOX NPs and Ce6 + PPE-*TK*-DOX NPs sig-nificantly increased the areas under the curve (AUCs) in blood 10.55-fold and 11.27-fold greater than free DOX, respectively (Fig. S10).

The biodistribution and tumor accumulation of Ce6@PPE-*TK*-DOX NPs were further examined in mice bearing MDA-MB-231 tumors. As reported, photosensitizer Ce6 can serve as a chelating agent to capture gadolinium-III (Gd^{3+}) [41], enabling T_1-contrast in magnetic resonance (MR) imaging, and the strong fluorescence of Ce6 can be utilized for fluorescence imaging of tumors. Therefore, cross-section T_1 MR imaging was first performed in the MDA-MB-231 xenograft mouse model after intravenous injection of the Ce6-Gd@PPE-*TK*-DOX, and the commercial agent Magnevist DTPA-Gd complex was used as a control. As shown in Fig. 5C, increased T_1 MR signal intensity appeared in the tumors of mice treated with Ce6-Gd@PPE-*TK*-DOX at 2 h post-injection, and the strongest MR signals were observed at 6 h post-injection. Next, the MR signal intensity declined gradually due to blood clearance. In addition, stronger MR signals of Ce6-Gd@PPE-*TK*-DOX were observed at all three time points than those of the commercial agent DTPA-Gd, likely due to
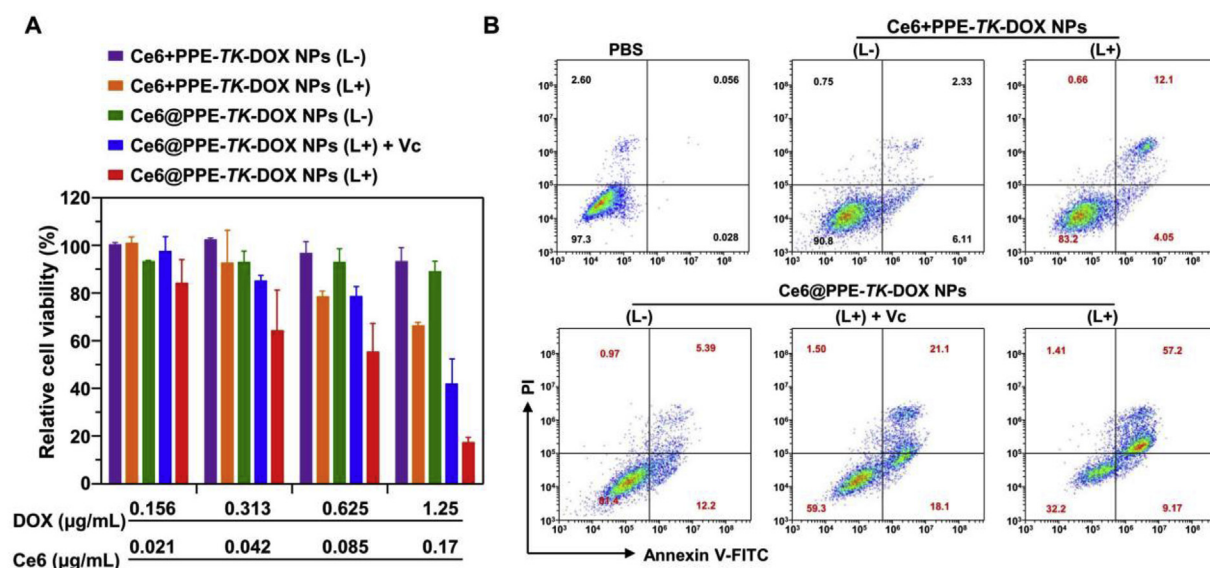
Fig. 4. The phototriggered intracellular prodrug release and activation significantly enhanced the tumor cell growth inhibition and cell apoptosis. (A) Relative cell viability of MDA-MB-231 cells after incubation with Ce6@PPE-*TK*-DOX NPs or control formulations with or without 660-nm laser irradiation (0.1 W/cm^2, 30 min). The MDA-MB-231 cells were pre-cultured with these formulations for 4 h. (B) Flow cytometric analysis of MDA-MB-231 cell apoptosis induced by different treatments at an equivalent DOX concentration of 1.25 μg/mL.

passive targeting of the nanoparticles by the tumor because of the EPR effect.

Furthermore, *in vivo* fluorescence imaging was performed by detecting Ce6 fluorescence at different time points after injection of Ce6@PPE-*TK*-DOX using a Xenogen IVIS® Lumina system. The fluorescence signals exhibited extensive distribution in the whole mouse body within 1 h post-injection, likely due to the high concentration of the nanoparticles in blood vessels. Thereafter, the Ce6 fluorescence signal intensity at the tumor site increased and reached a peak value at 4 h post-injection (Fig. 5D), indicating the gradual accumulation of Ce6@
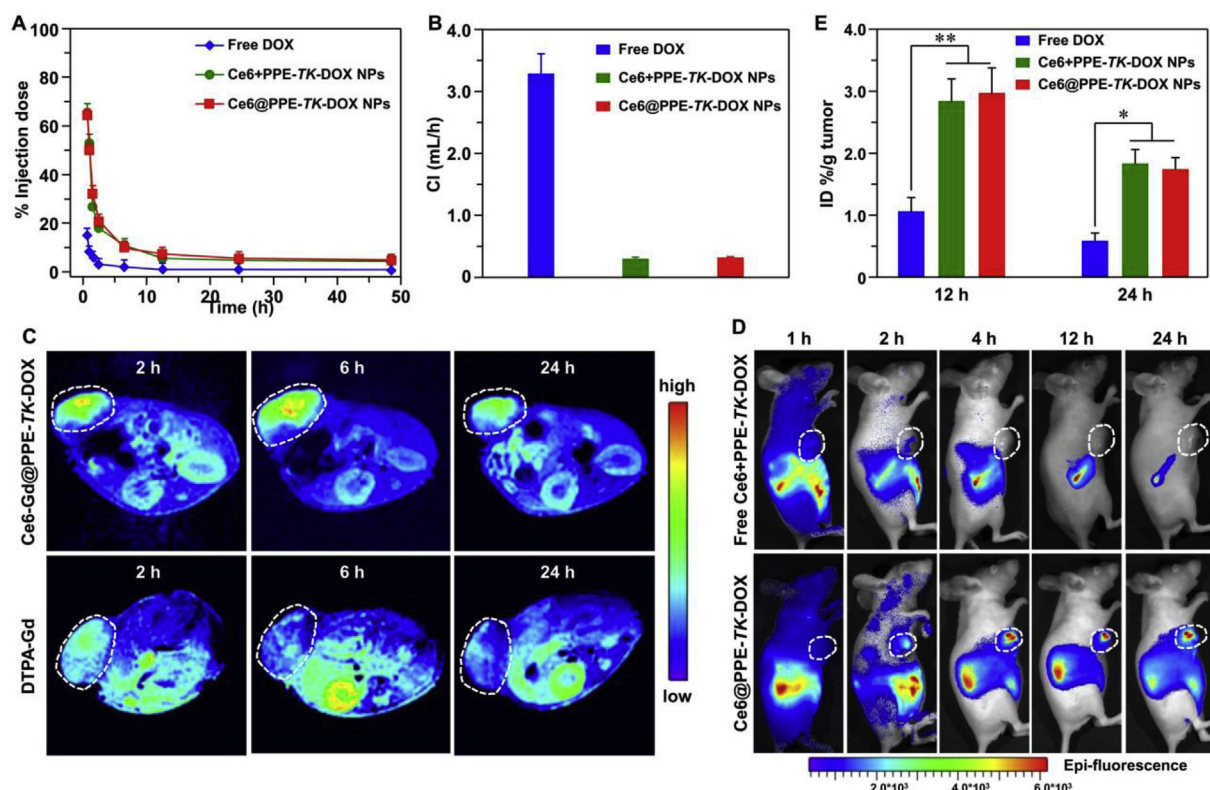

Fig. 5. The precise fluorescence/MR imaging of tumor tissue by the Ce6@PPE-*TK*-DOX NPs. (A) Plasma DOX concentration *versus* time after intravenous injection of Ce6@PPE-*TK*-DOX NPs, Ce6 + PPE-*TK*-DOX NPs, and free DOX. (B) The clearance rate (Cl) calculated from the pharmacokinetic curve (Fig. 5A). (C) T_1 MR images and (D) fluorescence images of MDA-MB-231 xenograft-bearing mice after intravenous (i.v.) injection of Ce6@PPE-*TK*-DOX NPs. (E) The quantification of DOX content in tumors 24 h post-injection. *p < 0.05, **p < 0.01. Relative viabilities of MDA-MB-231 cells after incubation with aforementioned formulations with or without NIR laser irradiation. *p < 0.05, **p < 0.01.

PPE-*TK*-DOX NPs in the tumor. Additionally, at 48 h post-injection, the mice were sacrificed, and the main organs and tumor tissue were collected for Xenogen IVIS® Lumina system analysis. As shown in Fig. S11, the mice treated with Ce6@PPE-*TK*-DOX exhibited strong Ce6 fluorescence in the tumor tissue, and the fluorescence signals of Ce6 were also clearly detected in the kidney and liver.

In addition, DOX accumulation in the tumor tissue and main organs was quantitatively measured. Mice bearing MDA-MB-231 tumors were intravenously injected with Ce6@PPE-*TK*-DOX NPs, Ce6 + PPE-*TK*-DOX NPs or free DOX at an equivalent DOX dosage of 5.0 mg/kg. Next, the mice were sacrificed, and the main organs and tumor tissue were collected for UPLC analysis. As shown in Fig. 5E, comparable DOX accumulation in tumor tissues was observed at either 12 or 24 h post-injection of Ce6@PPE-*TK*-DOX NPs and Ce6 + PPE-*TK*-DOX NPs (Fig. 5E) and was significantly higher than that of free DOX. Additionally, both nanoparticles showed similar DOX accumulation in main organs (Fig. S12), including the heart, liver, spleen, lung, and kidney, likely because of the similar physicochemical properties of both formulations.

Encouraged by the phototriggered prodrug release and precise fluorescence/MR imaging of tumor tissue, we further evaluated the antitumor efficacy of Ce6@PPE-*TK*-DOX NPs. Mice bearing MDA-MB-231 tumors were intravenously injected with Ce6@PPE-*TK*-DOX NPs, Ce6 + PPE-*TK*-DOX NPs or free DOX at an equivalent DOX dosage of 5.0 mg/kg. Under the guidance of fluorescence and MR dual-modal imaging, the whole tumor tissue area was precisely irradiated with a 660-nm laser 6 h post-injection; the subset of mice not treated with light irradiation was used as the control. Fig. 6A demonstrated that the mice treated with Ce6 + PPE-*TK*-DOX NPs(L+) only showed moderate inhibition of tumor growth, with no significant differences between the formulations. The cause might be that the insufficient accumulation of free Ce6 resulted in inefficient DOX prodrug release. In contrast, treatment with Ce6@PPE-*TK*-DOX NPs(L+) significantly elevated tumor inhibition and exhibited the greatest improvement in antitumor efficiency, validating the efficiently enhanced anticancer efficacy by phototriggered DOX prodrug release. In addition, inspection of the

tumor weights summarized in Fig. 6B and final tumor growth rates in Fig. 6C indicated that the Ce6@PPE-*TK*-DOX NPs(L+) group exhibited the highest anticancer efficacy. Moreover, cell proliferation in the tumor tissues was analyzed by immunohistochemical staining after treatment. The lowest percentage of proliferating tumor cells induced by treatment with Ce6@PPE-*TK*-DOX NPs(L+) was confirmed by PCNA staining of the tumor sections, verifying that phototriggered DOX prodrug could achieve superior anticancer efficacy (Fig. 6D).

According to our design, the Ce6@PPE-*TK*-DOX NPs could stably hold the prodrug in the bloodstream and healthy tissue to minimize drug leakage and reduce cytotoxic effects. Therefore, the biosafety of Ce6@PPE-*TK*-DOX NPs was evaluated by monitoring the body weight change during the whole therapy period. The Ce6@PPE-*TK*-DOX NPs with or withour light irradiation did not lead to remarkable body weight loss during treatment (Fig. S13), suggesting the negligible toxicity of this prodrug delivery system. Moreover, the pathological sections of main organs were analyzed by hematoxylin and eosin (H&E) staining (Fig. S14). The Ce6@PPE-*TK*-DOX NPs with or withour light irradiation showed negligible toxic effects on the heart, liver, spleen, and kidney, further confirming the excellent biocompatibility of such phototriggered prodrug systems.

4. Conclusion

In summary, we have successfully designed and explored Ce6@PPE-*TK*-DOX NPs with phototriggered prodrug release and activation for cancer therapy. The DOX prodrug was covalently conjugated into the side groups of the polyphosphoester *via* the ROS-sensitive TK bond, and the synthesized PPE-*TK*-DOX was co-self-assembled with Ce6 to form nanodrug Ce6@PPE-*TK*-DOX NPs. The high stability of the TK bond under physiological conditions efficiently prevented premature drug leakage at off-target sites, minimizing the side effect in healthy tissue and cells. After circulating into the tumor interstitium, under the guidance of fluorescence/MR dual-model imaging, the precise 660-nm red light irradiation induced ROS generation, which rapidly cleaved the TK
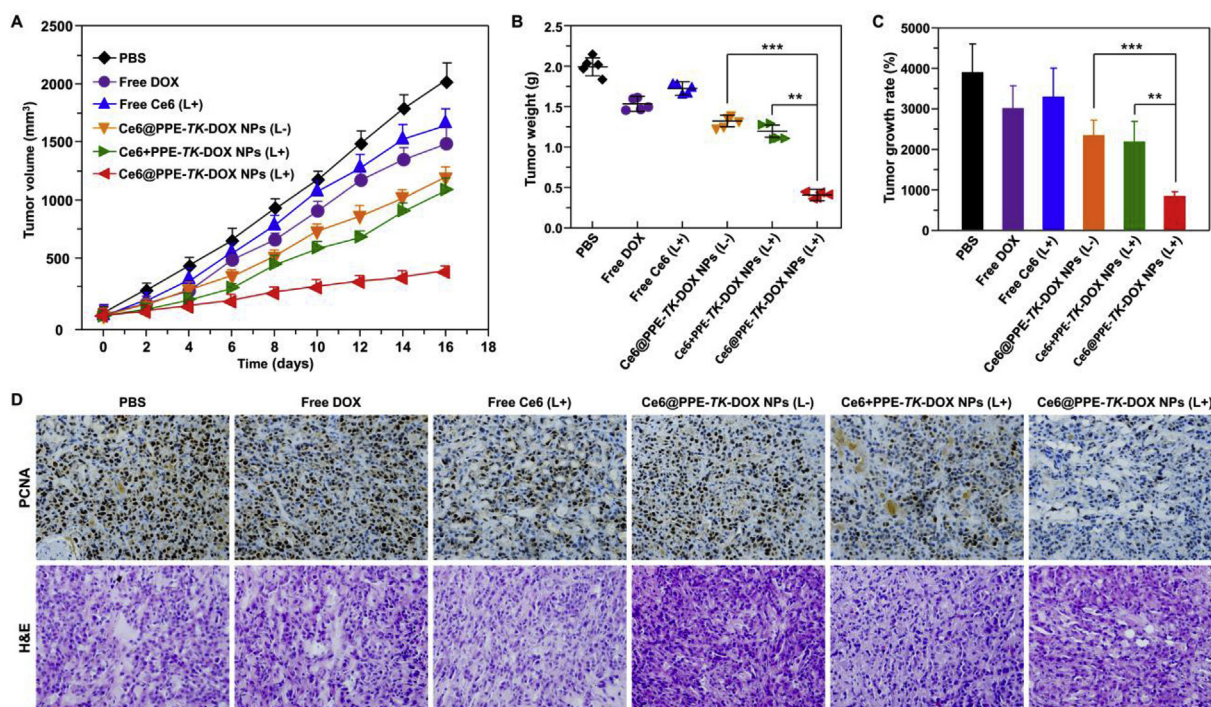

Fig. 6. The phototriggered intracellular prodrug release and activation to realize superior anticancer efficacy of Ce6@PPE-*TK*-DOX NPs. (A, C) The MDA-MB-231 tumor growth curves (A) and tumor growth rates (C) of various groups after intravenous administration. The tumor site was irradiation with 660-nm laser (0.1 W/cm², 30 min) 6 h post-injection. Data are presented as the mean ± SD, n = 5. (B) Weights of MDA-MB-231 xenograft tumors at the last time point of treatment. (D) PCNA and H&E analyses of tumor tissues after treatment, as indicated.

bond between DOX and PPE. Therefore, the DOX prodrug was locoregionally released and activated for tumor-specific drug delivery with high controllability by light. Taken together, such a phototriggered prodrug release and activation strategy significantly enhances the therapeutic efficacy of nanomedicine and minimizes the size effect, providing new avenues to fabricate the next generation of nanodrugs with good biosafety and superior antitumor efficiency in cancer treatment.

Conflict of Interest

The authors declare no competing financial interest.

Acknowledgements

Appendix A. Supplementary data

Supplementary data to this article can be found online at https://doi.org/10.1016/j.biomaterials.2018.10.010.

References

[1] S. Wilhelm, A.J. Tavares, Q. Dai, S. Ohta, J. Audet, H.F. Dvorak, W.C.W. Chan, Analysis of nanoparticle delivery to tumours, Nat. Rev. Mater. 1 (2016) 16014.

[2] D.L. Wang, Y. Jin, X.Y. Zhu, D.Y. Yan, Synthesis and applications of stimuli-responsive hyperbranched polymers, Prog. Polym. Sci. 64 (2017) 114–153.

[3] H. Cabral, K. Kataoka, Progress of drug-loaded polymeric micelles into clinical studies, J. Contr. Release 190 (2014) 465–476.

[4] J. Wang, S. Shen, D. Li, C. Zhan, Y. Yuan, X. Yang, Photoswitchable Ultrafast transactivator of transcription (TAT) targeting effect for nanocarrier-based on-demand drug delivery, Adv. Funct. Mater. 28 (2018) 1704806.

[5] S.Y. Qin, A.Q. Zhang, S.X. Cheng, L. Rong, X.Z. Zhang, Drug self-delivery systems for cancer therapy, Biomaterials 112 (2017) 234–247.

[6] Y. Li, K. Xiao, W. Zhu, W. Deng, K.S. Lam, Stimuli-responsive cross-linked micelles for on-demand drug delivery against cancers, Adv. Drug Deliv. Rev. 66 (2014) 58–73.

[7] D. Liu, F. Yang, F. Xiong, N. Gu, The smart drug delivery system and its clinical potential, Theranostics 6 (2016) 1306–1323.

[8] D. Li, Y. Ma, J. Du, W. Tao, X. Du, X. Yang, J. Wang, Tumor acidity/NIR controlled interaction of transformable nanoparticle with biological systems for cancer therapy, Nano Lett. 17 (2017) 2871–2878.

[9] M. Kanamala, W.R. Wilson, M. Yang, B.D. Palmer, Z. Wu, Mechanisms and biomaterials in pH-responsive tumour targeted drug delivery: a review, Biomaterials 85 (2016) 152–167.

[10] M. Karimi, P.S. Zangabad, S. Baghaee-Ravari, M. Ghazadeh, H. Mirshekari, M.R. Hamblin, Smart nanostructures for cargo delivery: uncaging and activating by light, J. Am. Chem. Soc. 139 (2017) 4584–4610.

[11] C. Qian, J. Yu, Y. Chen, Q. Hu, X. Xiao, W. Sun, C. Wang, P. Feng, Q.D. Shen, Z. Gu, Light-activated hypoxia-responsive nanocarriers for enhanced anticancer therapy, Adv. Mater. 28 (2016) 3313–3320.

[12] V.P. Torchilin, Nat. Rev. Multifunctional, stimuli-sensitive nanoparticulate systems for drug delivery, Drug Discov. 13 (2014) 813–827.

[13] X.Z. Yang, X.J. Du, Y. Liu, Y.H. Zhu, Y.Z. Liu, Y.P. Li, J. Wang, Rational design of polyion complex nanoparticles to overcome cisplatin resistance in cancer therapy, Adv. Mater. 26 (2014) 931–936.

[14] F. Zhou, B. Feng, T. Wang, D. Wang, Z. Cui, S. Wang, C. Ding, Z. Zhang, J. Liu, H. Yu, Y. Li, Programmed multiresponsive vesicles for enhanced tumor penetration and combination therapy of triple-negative breast cancer, Adv. Funct. Mater. 27 (2017) 1606530.

[15] X. Xu, P.E. Saw, W. Tao, Y. Li, X. Ji, S. Bhasin, Y. Liu, D. Ayyash, J. Rasmussen, M. Huo, J. Shi, O.C. Farokhzad, ROS-responsive polyprodrug nanoparticles for triggered drug delivery and effective cancer therapy, Adv. Mater. 29 (2017) 1700141.

[16] K. Ulbrich, K. Hola, V. Subr, A. Bakandritsos, J. Tucek, R. Zboril, Targeted drug delivery with polymers and magnetic nanoparticles: covalent and noncovalent approaches, release control, and clinical studies, Chem. Rev. 116 (2016) 5338–5431.

[17] C. Luo, J. Sun, D. Liu, B.J. Sun, L. Miao, S. Musetti, J. Li, X.P. Han, Y.Q. Du, L. Li, L. Huang, Z.G. He, Self-assembled redox dual-responsive prodrug-nanosystem formed by single thioether-bridged paclitaxel-fatty acid conjugate for cancer chemotherapy, Nano Lett. 16 (2016) 5401–5408.

[18] J. Yang, S. Zhai, H. Qin, H. Yan, D. Xing, X. Hu, NIR-controlled morphology transformation and pulsatile drug delivery based on multifunctional phototheranostic nanoparticles for photoacoustic imaging-guided photothermal-chemotherapy, Biomaterials 176 (2018) 1–12.

[19] Y.C. Ma, J.X. Wang, W. Tao, C.Y. Sun, Y.C. Wang, D.D. Li, F. Fan, H.S. Qian, X.Z. Yang, Redox-responsive polyphosphoester-based micellar nanomedicines for overriding chemoresistance in breast cancer cells, ACS Appl. Mater. Interfaces 7 (2015) 26315–26325.

[20] X. Wei, Q. Luo, L. Sun, X. Li, H. Zhu, P. Guan, M. Wu, K. Luo, Q. Gong, Enzyme-and pH-sensitive branched polymer-doxorubicin conjugate-based nanoscale drug delivery system for cancer therapy, ACS Appl. Mater. Interfaces 8 (2016) 11765–11778.

[21] H.J. Han, D. Valdeperez, Q. Jin, B. Yang, Z.H. Li, Y.L. Wu, B. Pelaz, W.J. Parak, J. Ji, Dual enzymatic reaction-assisted gemcitabine delivery systems for programmed pancreatic cancer therapy, ACS Nano 11 (2017) 1281–1291.

[22] W. He, X. Hu, W. Jiang, R. Liu, D. Zhang, J. Zhang, Z. Li, Y. Luan, Rational design of a new self-codelivery system from redox-sensitive camptothecin-cytarabine conjugate assembly for effectively synergistic anticancer therapy, Adv. Healthc. Mater. 6 (2017) 1700829.

[23] Y. Zhang, J. Ding, M. Li, X. Chen, C. Xiao, X. Zhuang, Y. Huang, X. Chen, One-step "click chemistry"-synthesized cross-linked prodrug nanogel for highly selective intracellular drug delivery and upregulated antitumor efficacy, ACS Appl. Mater. Interfaces 8 (2016) 10673–10682.

[24] H. Wei, R.X. Zhuo, X.Z. Zhang, Design and development of polymeric micelles with cleavable links for intracellular drug delivery, Prog. Polym. Sci. 38 (2013) 503–535.

[25] M.R. Junttila, F.J. de Sauvage, Influence of tumour micro-environment heterogeneity on therapeutic response, Nature 501 (2013) 346–354.

[26] P.L. Bedard, A.R. Hansen, M.J. Ratain, L.L. Siu, Tumour heterogeneity in the clinic, Nature 501 (2013) 355–364.

[27] L. Cheng, C. Wang, L. Feng, K. Yang, Z. Liu, Functional nanomaterials for phototherapies of cancer, Chem. Rev. 114 (2014) 10869–10939.

[28] A.Y. Rwei, W. Wang, D.S. Kohane, Photoresponsive nanoparticles for drug delivery, Nano Today 10 (2015) 451–467.

[29] M. Karimi, A. Ghasemi, P.S. Zangabad, R. Rahighi, S.M.M. Basri, H. Mirshekari, M. Amiri, Z.S. Pishabad, A. Aslani, M. Bozorgomid, D. Ghosh, A. Beyzavi, A. Vaseghi, A.R. Aref, L. Haghani, S. Bahrami, M.R. Hamblin, Smart micro/nanoparticles in stimulus-responsive drug/gene delivery systems, Chem. Soc. Rev. 45 (2016) 1457–1501.

[30] J. Li, C. Sun, W. Tao, Z. Cao, H. Qian, X. Yang, J. Wang, Photoinduced PEG deshielding from ROS-sensitive linkage-bridged block copolymer-based nanocarriers for on-demand drug delivery, Biomaterials 170 (2018) 147–155.

[31] G. Yang, X. Sun, J. Liu, L. Feng, Z. Liu, Light-responsive, singlet-oxygen-triggered on-demand drug release from photosensitizer-doped mesoporous silica nanorods for cancer combination therapy, Adv. Funct. Mater. 26 (2016) 4722–4732.

[32] J.J. Hu, Q. Lei, M.Y. Peng, D.W. Zheng, Y.X. Chen, X.Z. Zhang, A positive feedback strategy for enhanced chemotherapy based on ROS-triggered self-accelerating drug release nanosystem, Biomaterials 128 (2017) 136–146.

[33] M. Gao, F. Fan, D. Li, Y. Yu, K. Mao, T. Sun, H. Qian, W. Tao, X. Yang, Tumor acidity-activatable TAT targeted nanomedicine for enlarged fluorescence/magnetic resonance imaging-guided photodynamic therapy, Biomaterials 133 (2017) 165–175.

[34] S. Xu, X. Zhu, C. Zhang, W. Huang, Y. Zhou, D. Yan, Oxygen and Pt(II) Self-generating conjugate for synergistic photo-chemo therapy of hypoxic tumor, Nat. Commun. 9 (2018) 2053.

[35] Z. Cao, Y. Ma, C. Sun, Z. Lu, Z. Yao, J. Wang, D. Li, Y. Yuan, X. Yang, ROS-sensitive polymeric nanocarriers with red light-activated size shrinkage for remotely controlled drug release, Chem. Mater. 30 (2018) 517–525.

[36] C.Y. Sun, Z. Cao, X.J. Zhang, R. Sun, C.S. Yu, X. Yang, Cascade-amplifying synergistic effects of chemo-photodynamic therapy using ROS-responsive polymeric nanocarriers, Theranostics 8 (2018) 2939–2953.

[37] M. Wang, S. Sun, C.I. Neufeld, B. Perez-Ramirez, Q. Xu, Reactive oxygen species-responsive protein modification and its intracellular delivery for targeted cancer therapy, Angew. Chem. Int. Ed. 53 (2014) 13444–13448.

[38] V.G. Deepagan, S. Kwon, D.G. You, V.Q. Nguyen, W. Um, H. Ko, H. Lee, D.G. Jo, Y.M. Kang, J.H. Park, In situ diselenide-crosslinked polymeric micelles for ROS-mediated anticancer drug delivery, Biomaterials 103 (2016) 56–66.

[39] J.Z. Du, D.P. Chen, Y.C. Wang, C.S. Xiao, Y.J. Lu, J. Wang, G.Z. Zhang, Synthesis and micellization of amphiphilic brush-coil block copolymer based on poly(epsilon-caprolactone) and PEGylated polyphosphoester, Biomacromolecules 7 (2006) 1898–1903.

[40] C.Y. Sun, S. Dou, J.Z. Du, X.Z. Yang, Y.P. Li, J. Wang, Doxorubicin conjugate of poly (ethylene glycol)-block polyphosphoester for cancer therapy, Adv. Healthc. Mater. 3 (2014) 261–272.

[41] H. Gong, Z. Dong, Y. Liu, S. Yin, L. Cheng, W. Xi, J. Xiang, K. Liu, Y. Li, Z. Liu, Erratum: engineering of multifunctional nano-micelles for combined photothermal and photodynamic therapy under the guidance of multimodal imaging, Adv. Funct. Mater. 24 (2014) 6492–6502.